Acta Pharmaceutica Sinica B 2022;12(5):2578–2591

Chinese Pharmaceutical Association
Institute of Materia Medica, Chinese Academy of Medical Sciences

Acta Pharmaceutica Sinica B

www.elsevier.com/locate/apsb
www.sciencedirect.com

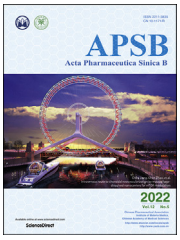

ORIGINAL ARTICLE

Self-assembling protein nanocarrier for selective delivery of cytotoxic polypeptides to CXCR4$^+$ head and neck squamous cell carcinoma tumors

Elisa Rioja-Blanco[a,b], Irene Arroyo-Solera[a,b,c], Patricia Álamo[a,b,c], Isolda Casanova[a,b,c], Alberto Gallardo[a,d], Ugutz Unzueta[a,b,c], Naroa Serna[c,e,f], Laura Sánchez-García[c,e,f], Miquel Quer[c,g], Antonio Villaverde[c,e,f], Esther Vázquez[c,e,f,*], Ramon Mangues[a,b,c,*], Lorena Alba-Castellón[a,b,*], Xavier León[c,g]

[a]*Institut d'Investigació Biomèdica Sant Pau (IIB-Sant Pau), Barcelona 08041, Spain*
[b]*Institut de Recerca contra la Leucèmia Josep Carreras, Barcelona 08025, Spain*
[c]*CIBER de Bioingeniería, Biomateriales y Nanomedicina (CIBER-BBN), Madrid 28029, Spain*
[d]*Department of Pathology, Hospital de la Santa Creu i Sant Pau, Barcelona 08041, Spain*
[e]*Institut de Biotecnologia i de Biomedicina, Universitat Autònoma de Barcelona, Bellaterra 08193, Spain*
[f]*Departament de Genètica i de Microbiologia, Universitat Autònoma de Barcelona, Bellaterra 08193, Spain*
[g]*Department of Otorhinolaryngology, Hospital de la Santa Creu i Sant Pau, Barcelona 08041, Spain*

Received 5 July 2021; received in revised form 3 September 2021; accepted 15 September 2021

KEY WORDS

Targeted drug delivery;
Protein nanoparticles;
CXCR4 receptor;
HNSCC;
Cell targeting;
Recombinant proteins;
Nanotoxins;
Cancer therapy

Abstract Loco-regional recurrences and distant metastases represent the main cause of head and neck squamous cell carcinoma (HNSCC) mortality. The overexpression of chemokine receptor 4 (CXCR4) in HNSCC primary tumors associates with higher risk of developing loco-regional recurrences and distant metastases, thus making CXCR4 an ideal entry pathway for targeted drug delivery. In this context, our group has generated the self-assembling protein nanocarrier T22-GFP-H6, displaying multiple T22 peptidic ligands that specifically target CXCR4. This study aimed to validate T22-GFP-H6 as a suitable nanocarrier to selectively deliver cytotoxic agents to CXCR4$^+$ tumors in a HNSCC model. Here we demonstrate that T22-GFP-H6 selectively internalizes in CXCR4$^+$ HNSCC cells, achieving a high accumulation in CXCR4$^+$ tumors *in vivo*, while showing negligible nanocarrier distribution in non-tumor bearing organs. Moreover, this T22-empowered nanocarrier can incorporate bacterial toxin domains to generate therapeutic nanotoxins that induce cell death in CXCR4-overexpressing tumors in the absence

*Corresponding authors. Tel.: +34 935537919 (Ramon Mangues); +34 935537921 (Lorena Alba-Castellón).
E-mail addresses: esther.vazquez@uab.cat (Esther Vázquez), rmangues@santpau.cat (Ramon Mangues), lalba@santpau.cat (Lorena Alba-Castellón).
Peer review under responsibility of Chinese Pharmaceutical Association and Institute of Materia Medica, Chinese Academy of Medical Sciences

https://doi.org/10.1016/j.apsb.2021.09.030

of histological alterations in normal organs. Altogether, these results show the potential use of this T22-empowered nanocarrier platform to incorporate polypeptidic domains of choice to selectively eliminate CXCR4$^+$ cells in HNSCC. Remarkably, to our knowledge, this is the first study testing targeted protein-only nanoparticles in this cancer type, which may represent a novel treatment approach for HNSCC patients.

1. Introduction

Head and neck squamous cell carcinoma (HNSCC) is the sixth most common cancer worldwide, accounting for more than 650,000 cases and 330,000 deaths annually[1,2]. Current treatment allows loco-regional control of the disease[3,4], however, up to 60% of patients develop loco-regional recurrences and up to 30% distant metastases after treatment, with a median overall survival of less than one year[5]. Importantly, loco-regional recurrences and distant metastases represent the main cause of patient mortality[6]. Despite the improvement in the treatment, including novel surgical procedures, radiotherapy, new cytostatic compounds, targeted monoclonal antibodies, and immunotherapy; up to 30%−40% of HNSCC patients still die as a consequence of the disease[5]. Thus, new therapeutic strategies are urgently needed in order to improve patient survival.

In the last years, targeted-drug delivery to cancer cells has emerged as a promising alternative to existing treatments, as it potentially improves drug accumulation within tumor tissues, thus enhancing response rates while reducing side effects[7,8]. In this regard, the chemokine receptor 4 (CXCR4) has been proposed as a promising molecular target. CXCR4 is overexpressed in a wide range of cancers, including HNSCC and has been related to enhanced invasion, migration, and angiogenesis, as well as with a stem cell phenotype, chemotherapy resistance and metastasis development[9,10]. Importantly, our group and others have reported that CXCR4 overexpression in HNSCC primary tumors associates with a higher risk of developing loco-regional recurrences and distant metastases as well as with worse patient prognosis[11,12].

In this context, our group has developed the self-assembling protein nanocarrier T22-GFP-H6. This nanocarrier incorporates T22, a cationic peptide that acts as a CXCR4 antagonist, designed to inhibit HIV infection[13]. In our case, T22 was used instead as a peptidic ligand to specifically target the CXCR4 receptor, fused to the green fluorescent protein (GFP), allowing its follow up both *in vitro* and *in vivo*[14,15]; and a polyhistidine tag (H6) necessary for T22-GFP-H6 purification and conformation[16,17]. T22-GFP-H6 nanocarrier has already proved to be effective in targeting CXCR4$^+$ cells in colorectal cancer (CRC) and diffuse large B-cell lymphoma (DLBCL) animal models[15,18]. Remarkably, so far, no protein-based nanocarrier has been reported to selectively target HNSCC cancer cells, highlighting the relevance of this study. Moreover, T22-GFP-H6 displays great versatility as a vehicle allowing the conjugation of different chemical drugs or the incorporation of toxin domains, enabling the selective targeting and depletion of CXCR4$^+$ cancer cells[19]. Considering the implication of CXCR4 in loco-regional recurrence and distant metastases, this approach could potentially improve current HNSCC treatment.

In this study, we report that T22-GFP-H6 nanocarrier internalizes selectively in CXCR4$^+$ HNSCC cell lines. Moreover, when administered *in vivo* in a subcutaneous CXCR4-overexpressing HNSCC model, T22-GFP-H6 mostly accumulates in the tumor compared to other non-tumor bearing organs. Finally, we show the ability of the nanocarrier to selectively deliver cytotoxic agents to CXCR4$^+$ tumors. For this purpose, we intravenously administered T22-DITOX-H6 and T22-PE24-H6, two nanoparticles presenting the same multidomain-based design as T22-GFP-H6 nanocarrier but carrying the diphtheria toxin catalytic domain and the *Pseudomonas aeruginosa* exotoxin A domain, respectively. Both nanotoxins were able to induce cancer cell death and achieve a potent antitumor effect in CXCR4-overexpressing tumors in HNSCC mouse models, proving their suitability as targeted nanoparticles for anticancer therapy. This work highlights the potential use of T22-GFP-H6 derived nanoparticles to selectively target CXCR4$^+$ cells in HNSCC patients with worse prognosis.

2. Materials and methods

2.1. Nanoparticles production, purification, and characterization

T22-GFP-H6, T22-PE24-H6 and T22-DITOX-H6 production and purification were described in previous work[14,15,19]. Coding sequences introduced in the plasmid pET22b (Novagen 69744-3) for the three nanoparticles are included in Supporting Information Fig. S1.

2.2. Cell lines and cell culture

HNSCC cell lines UM-SCC-74B (74B) and UM-SCC-22A (22A)[20] were kindly provided by Dr. R.H. Brakenhoff and Dr. Gregory Oakley, respectively. 293T cell lines were purchased from ATCC. HNSCC cell lines were authenticated using the Cell ID Kit (Promega, Madison, WI, USA). The short tandem repeat (STR) profiles were compared with the profiles previously described[21]. All cell lines were cultured in Dulbecco's modified Eagle's medium (DMEM) containing 10% Fetal Bovine Serum (FBS), 100 U/mL penicillin/streptomycin and 2 mmol/L glutamine (Life Technologies) and incubated at 37 °C and 5% CO_2 in a humidified atmosphere.

2.3. Lentiviral CXCR4-Luciferase and Luciferase transduction

Lentiviral plasmid CXCR4-Luciferase (pLenti-III-UbC-CXCR4-2A-luc) and Luciferase (pLenti-III-UbC-luc) were purchased from Abm (Abm, Vancouver, Canada). Lentiviral particles were obtained by co-transfection of the plasmids described above with pMD.G_VSV G-poly-A vector and p8 91-Gag-Pol vector into 293T cells using lipofectamine 2000 (Life Technologies). After 48 h, cell supernatant was harvested, filtered through a 45 μm filter and used to transduce UM-SCC-74B (74B) and UM-SCC-22A (22A) cell lines. Infected cell lines were selected in medium containing puromycin (0.8 μg/mL for 74B and 0.4 μg/mL for

22A) for 3−4 weeks until stable clones were obtained. Cell lines transduced with the CXCR4-Luciferase plasmid (74B-CXCR4$^+$ and 22A-CXCR4$^+$) were sorted by FACSAria cell sorter (BD Biosciences) using PE-Cy5 mouse antihuman CXCR4 monoclonal antibody (BD Biosciences) to isolate membrane CXCR4-overexpressing cells.

2.4. Flow cytometry

CXCR4 membrane expression in the cell lines was determined by FACSCalibur (BD Biosciences) using PE-Cy5 mouse anti-human CXCR4 monoclonal antibody (BD Biosciences). The negative population was defined using the PE-Cy5 Mouse IdG2a isotype (BD Biosciences) as a control.

T22-GFP-H6 internalization was quantified by GFP fluorescence signal using FACSCalibur (BD Biosciences). Cells seeded in 6-well plates (250,000 cell/well for 74B and 500,000 cells/well for 22A) were treated with different T22-GFP-H6 concentrations (0−500 nmol/L) for different times (1, 6, and 24 h), then washed with PBS, detached from the plate, and trypsinized (1 mg/mL trypsin, Life Technologies) for 15 min at 37 °C in order to remove nonspecific binding of the nanocarrier. For the CXCR4 blocking assays, cells were preincubated with AMD3100 (1 μmol/L, Sigma) for 1 h before adding the nanocarrier. T22-GFP-H6 internalization data was analyzed using the Cell Quest Pro software and represented as mean fluorescence intensity (MFI). Buffer-treated cells were considered as the negative population. All experiments were performed in triplicate.

2.5. Western blotting

T22-GFP-H6 internalization was further studied by Western blotting (WB). For that, 74B-CXCR4$^+$ cells were incubated with different T22-GFP-H6 concentrations (1, 5, 10, and 20 nmol/L) for 1 h. Then, cells were washed with PBS and proteins were extracted using RIPA buffer (Sigma). Protein samples were then sonicated, centrifuged at top speed for 10 min at 4 °C, and supernatants were stored at −20 °C to perform Western blotting assays. Protein concentration was assessed using the Pierce™ Rapid Gold BCA Protein Assay Kit (Thermo Scientific) according to the manufacturer's instructions. 50 μg of protein extracts were loaded in a 15% SDS-PAGE gel and transferred to a nitrocellulose blotting membrane (GE Healthcare life sciences). Membranes were blocked with 5% skim milk in TBS-T for 1 h at room temperature and incubated overnight at 4 °C with the primary antibodies GFP rabbit polyclonal (1:500, Santa Cruz Biotechnology) or α/β-tubulin (1:1,000, Cell Signaling). After washing with TBS-T to remove nonspecific antibody binding, membranes were incubated with the corresponding secondary antibodies (1:10,000, Jackson Immune Research) for 1 h at room temperature. Finally, membranes were further washed with TBS-T and visualized with the SuperSignal™ West Pico Chemiluminescent Substrate (Thermo Scientific) and the ChemiDoc XRS$^+$ imaging system (Biorad).

2.6. Cell viability assays

The Cell Proliferation Kit II (XTT) (Roche) was used to determine the cytotoxicity of T22-DITOX-H6 and T22-PE24-H6 nanotoxins, according to the manufacturer's instructions. Cells seeded in 96-well plates (2500 cell/well) were treated with buffer or 50 nmol/L of either T22-DITOX-H6 or T22-PE24-H6 for different times (6, 24, and 48 h). To test the ability of the nanotoxins to exert any off-target cytotoxicity upon cellular content release, 74B-CXCR4$^+$ cells were seeded in 96-well plates and treated as previously explained. After 48 h, when cells were dead, supernatants were transferred to 74B mock 96-well plate cultures and further incubated for 48 h. After the different treatments, the XTT reagent was added to the plate and incubated at 37 °C for 4 h. After this incubation period, the absorbance, which directly correlates to the number of viable cells, was measured using a multi-well spectrophotometer (FLUOstar Optima, BMG Labtech). All experiments were performed in triplicate.

2.7. In vivo experiments

Four-week-old female Swiss nude mice [NU(Ico)-Foxn1^{nu}] weighing 18−25 g were purchased from Charles River (France). Animals were housed in a specific pathogen-free (SPF) environment with sterile food and water *ad libitum*. All animal experiments were approved by the Hospital de la Santa Creu i Sant Pau Animal Ethics Committee.

Subcutaneous tumor models were obtained injecting 10 million cells either 74B mock or 74B-CXCR4$^+$ in both flanks of the animal. Tumor size was measured three times per week with a caliper according to Eq. (1):

$$\text{Tumor volume} = \text{Width}^2 \times \text{Length}/2 \quad (1)$$

To assess T22-GFP-H6 biodistribution, animals bearing tumors of approximately 200 mm^3 were randomized into two groups ($n = 3$ per group). One group was injected intravenously with a single dose of 200 μg T22-GFP-H6, the other one with buffer (166 mmol/L $NaCO_3H$ pH 8). Animals were euthanized at different times post-injection (2, 6, and 24 h) and an *ex vivo* measurement of fluorescence intensity (FLI) of tumors and different organs was performed using IVIS® Spectrum 200 (PerkinElmer). For the CXCR4 blocking experiments, AMD3100 was subcutaneously injected into mice at a dose of 10 mg/kg three times (1 h before T22-GFP-H6 administration and 1 and 2 h after). After euthanizing the animals, tumors and organs were collected, fixed in 4% formaldehyde solution and paraffin-embedded. Plasma was also obtained by centrifugation of total blood, extracted from the animals by intracardiac puncture. Fluorescence intensity (FLI) data is expressed as average radiant efficiency and it has been calculated subtracting the FLI signal of buffer-treated mice to the FLI signal of T22-GFP-H6-treated animals. The FLI ratio was obtained by dividing the FLI signal of each organ by the FLI signal of the kidneys (organ with the most stable FLI signal throughout the experiment); thus being expressed as fold-change respect to kidneys.

T22-PE24-H6 and T22-DITOX-H6 cytotoxic effect was studied using the CXCR4 over-expressing subcutaneous mouse model described above ($n = 2$ per group). When tumors reached an approximate volume of 200 mm^3, 30 μg of T22-DITOX-H6 or 100 μg T22-PE24-H6 were intravenously administered to the animals. After either 24 or 48 h, animals were euthanized, and tumors and normal organs were collected and fixed for further analysis. For the antitumoral effect experiment, 2 million cells either 74B mock or 74B-CXCR4$^+$ were orthotopically injected in the tongue of the animals. After the detection of luminescence emitted by viable tumor cells, using IVIS® Spectrum 200, animals were randomized into three groups ($n = 5$ per group). Nanoparticle-treated animals were intravenously administered

10 μg of T22-DITOX-H6 or T22-PE24-H6 daily up to 5 doses. On alternate days, body weight was registered and tumor growth was measured by the luminescent signal emitted by tumor cells using IVIS® Spectrum 200 system. Mice were euthanized 24 h after the fifth dose. At the end point of the experiment, tumor volume was measured with a caliper according to Eq. (2):

$$\text{Tumor volume} = \text{Width} \times \text{Length} \times \text{Depth} \quad (2)$$

and tumors and organs were collected for histological analysis.

2.8. Confocal laser scanning microscopy

Colocalization of GFP and CXCR4 within tumor tissues, liver, and kidneys was performed by immunofluorescence. Paraffin-embedded tumors and organs were cut into 4 μm sections, heated for 1 h at 60 °C, dewaxed and rehydrated. Antigen retrieval was performed using Tris−EDTA Buffer, pH 9.0 (Invitrogen) in a Decloaking Chamber™ NxGen (Biocare medical) at 110 °C for 20 min. Then, samples were washed with TBS and blocked with TBS +0.5% TritonX-100 + 3% donkey serum for 1 h at room temperature. Tissue sections were then incubated with the primary antibodies GFP chicken IgY (1:250, AVES) and CXCR4 rabbit IgG (1:250, Abcam) overnight at 4 °C. Samples were washed and incubated with the secondary antibodies anti-chicken IgY-Cy2 (1:50, Jackson Immune Research) and anti-rabbit IgG-Alexa Fluor® 568 (1:200, abcam) for 2 h at room temperature. Finally, the tumor sections were washed, stained with DAPI 0.5 μg/mL for 10 min at RT, and mounted. Samples were visualized in a Confocal multi-spectral Leica SP5 AOBS microscope (Leica) and analyzed using Fiji, ImageJ software.

2.9. Histopathology, DAPI staining, and immunohistochemical analysis

In order to perform a histopathological analysis to assess any possible toxic effect, 4 μm paraffin-embedded tumor and organ sections were stained with H&E and analyzed by two independent observers (one section of the whole organ/tumor). Cell death in tumor tissues and normal organs was assessed by DAPI staining and cleaved caspase-3 immunohistochemical (IHC) staining (1:300, BD. Retrieval pH low, Dako). For DAPI staining, paraffin-embedded sections were dewaxed, rehydrated, and permeabilized with 0.5% Triton X-100. Then, slides were stained with DAPI mounting medium (ProLong™ Gold Antifade Mountant, Thermo Scientific) and visualized by fluorescence microscopy. Representative pictures were taken using an Olympus DP73 digital camera and the number of dead cells was quantified by counting the number of condensed nuclei per 10 high-power fields (magnification 400 ×). CXCR4 (1:200, Abcam, Retrieval pH high, Dako) expression was studied by immunohistochemistry (IHC) in cell pellets of the different HNSCC cell lines and tissue sections (tumor and non-tumor bearing organs). IHC staining was performed in a DAKO Autostainer Link48 following the manufacturer's instructions. Representative images were taken using an Olympus DP73 digital camera and processed with the Olympus CellD Imaging 3.3 software. CXCR4 expression levels in tumors and normal organs were quantified as mean gray values as well as cleaved caspase-3 positive cells using Fiji, ImageJ software.

2.10. Statistical analysis

Data are expressed as mean ± Standard Error. Statistical analyses were performed using the GraphPad Prism 5 software (GraphPad Software, San Diego, California USA). Results were analyzed by Student's *t*-test. Differences were considered statistically significant when P value < 0.05. All experiments were performed at least in triplicates.

3. Results

3.1. T22-GFP-H6 selectively internalizes in CXCR4-overexpressing HNSCC cells

CXCR4 cell membrane expression was assessed by flow cytometry and IHC (Supporting Information Fig. S2A–S2C) for 2 different HNSCC cell lines (74B mock and 74B-CXCR4$^+$, and 22A mock and 22A-CXCR4$^+$). 74B mock and 22A mock cell lines did not express CXCR4, whereas the CXCR4-overexpressing cell lines (74B-CXCR4$^+$ and 22A-CXCR4$^+$) presented CXCR4 located in the cell membrane. 22A-CXCR4$^+$ cell line showed the highest amounts of CXCR4 in the cell membrane as represented by its mean fluorescence intensity (MFI, Supporting Information Fig. S2B).

T22-GFP-H6 nanocarrier (Supporting Information Fig. S3) internalization inside the cells was measured by flow cytometry and represented as mean fluorescence intensity (MFI), which correlates with GFP presence inside the cells. Interestingly, T22-GFP-H6 only internalizes in the CXCR4-overexpressing cell lines, while MFI values for the mock cell lines remained similar to those observed in the buffer-treated cells (no statistically significant differences, Fig. 1A). Nanocarrier internalization was found to be concentration-dependant in both CXCR4-overexpressing cell lines (Fig. 1A). Moreover, T22-GFP-H6 internalization correlated with CXCR4 membrane expression, as MFI values were higher in the 22A-CXCR4$^+$ cell line compared to 74B-CXCR4$^+$ (Fig. 1A and Supporting Information Fig. S2B). T22-GFP-H6 internalization inside the cells was also assessed by WB confirming its entry to CXCR4$^+$ cells (Fig. 1B). No statistically significant differences were found in internalization at 1, 6 and 24 h (Fig. 1C and D). T22-GFP-H6 internalization appears to be fast and sustained in time in both CXCR4$^+$ cell lines.

Nanocarrier CXCR4 selective internalization was further corroborated by CXCR4 blockage using AMD3100 (CXCR4 antagonist). CXCR4-overexpressing cells pretreated with AMD3100 did not internalize the nanocarrier compared to the ones without AMD3100 (Fig. 1E and F). Thus, we have demonstrated that the T22-GFP-H6 nanocarrier internalizes within HNSCC cells *via* the CXCR4 receptor.

3.2. T22-GFP-H6 achieves a high tumor accumulation in subcutaneous HNSCC tumors compared to normal organs

T22-GFP-H6 tumor accumulation was measured after the administration of a 200 μg single-dose intravenous injection of the nanocarrier in CXCR4-overexpressing tumor-bearing mice. Animals were euthanized at different times (2, 6, and 24 h) and nanoparticle accumulation in tumors and normal organs was determined by GFP emitted fluorescence intensity using IVIS® Spectrum 200 system. T22-GFP-H6 was detectable in tumor tissue at the three studied time points, presenting a maximum at 6 h among the three studied time points (Fig. 2A). Importantly,

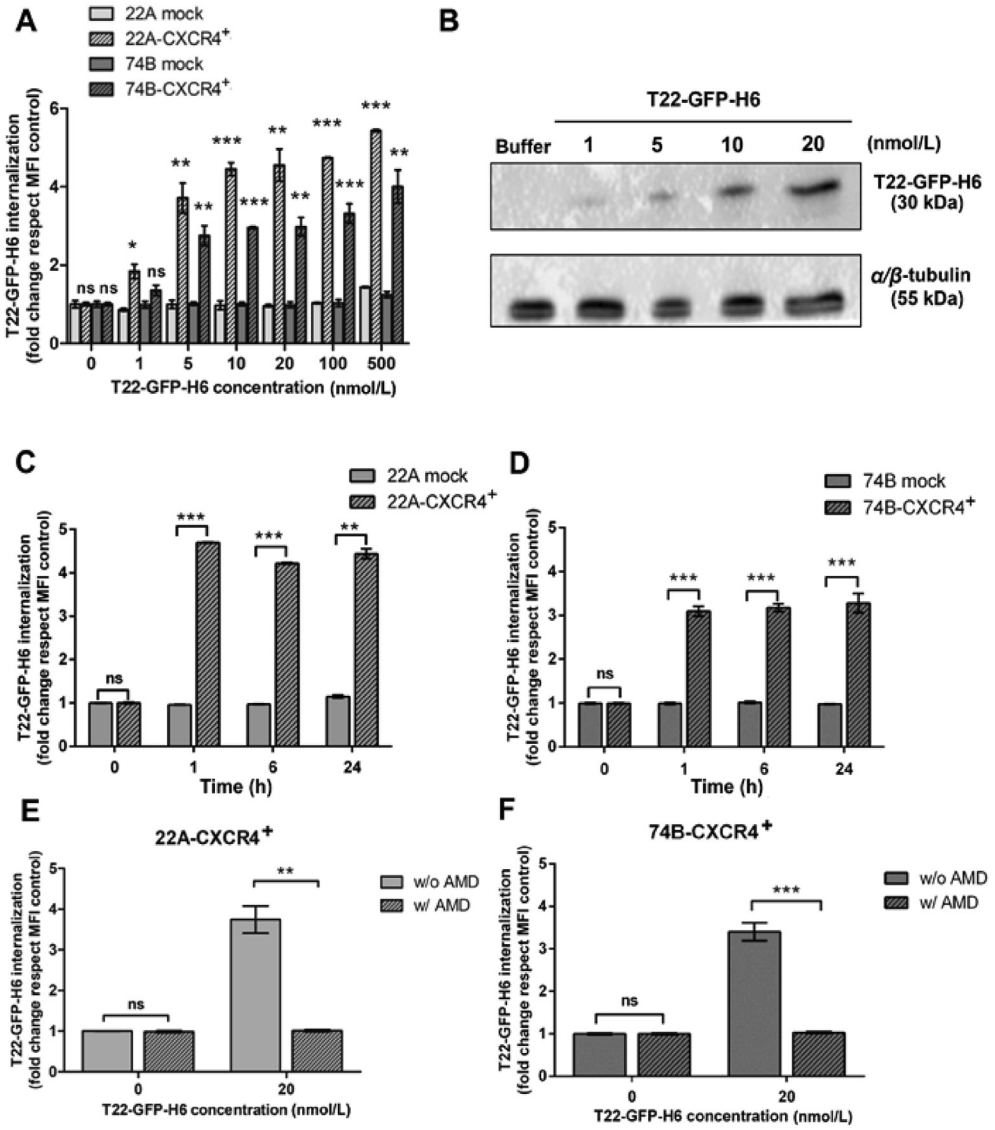

Figure 1 T22-GFP-H6 internalization in CXCR4$^+$ HNSCC cell lines *in vitro*. (A) T22-GFP-H6 intracellular levels in 22A mock, 22A-CXCR4$^+$, 74B mock, and 74B-CXCR4$^+$ cell lines quantified by flow cytometry after a 6h exposure at different concentrations (0−500 nmol/L) of the nanocarrier. (B) Western blotting assay showing the increasing accumulation of T22-GFP-H6 inside 74B-CXCR4$^+$ cells treated with different concentrations of the nanocarrier (1−20 nmol/L) for 1 h. (C) and (D) Nanocarrier internalization in 22A mock and 22A-CXCR4$^+$ (C) and 74B mock and 74B-CXCR4$^+$ (D) cells at three different incubation times (1, 6, and 24 h) in the presence of 20 nmol/L T22-GFP-H6. (E) and (F) AMD3100 blocking assay in 22A-CXCR4$^+$ (E) and 74B-CXCR4$^+$ (F) treated with a 20 nmol/L T22-GFP-H6 concentration. Data represented as mean ± Standard error. All experiments were performed in triplicate. *$P < 0.05$; **$P < 0.01$; ***$P < 0.001$; ns, non-significant. Statistical analysis performed by Student's *t*-test. MFI, mean fluorescence intensity.

nanocarrier accumulation was observed mainly in tumor tissues with almost no signal in non-tumor bearing organs (fold-change respect to kidneys below 1, indicated by the dashed line in Fig. 2B) (Fig. 2B and C). Remarkably, fluorescence intensity at 6 h was approximately 10-fold higher in tumor, when compared with the rest of the analyzed organs (Fig. 2B).

The area under the curve (AUC) was calculated for the time-course of the experiment in order to quantify the T22-GFP-H6 accumulation for the tumors and different healthy organs. Tumors accumulated 78.3 ± 11.8% of the total FLI measured in all organs (tumors and normal tissues, Fig. 2D and E). The rest of the organs reached distribution values lower than 10% (Fig. 2D and E). Importantly, the liver, an organ involved in the metabolism of drugs circulating in blood, presented a value lower than 1%.

T22-GFP-H6 biodistribution was found to be consistent with CXCR4 levels in each tissue, as measured by IHC (Fig. 3A and B). Tumor tissues displayed the highest expression of the receptor compared to non-tumor bearing organs, such as liver or kidneys (67- and 26-fold, respectively). Importantly, the spleen showed lower CXCR4 levels than tumors (4-fold), presenting a light pattern consistent with CXCR4 expression by immune cells such as lymphocytes. These results imply that the accumulation of the nanocarrier mainly in tumor tissues is driven by their high CXCR4

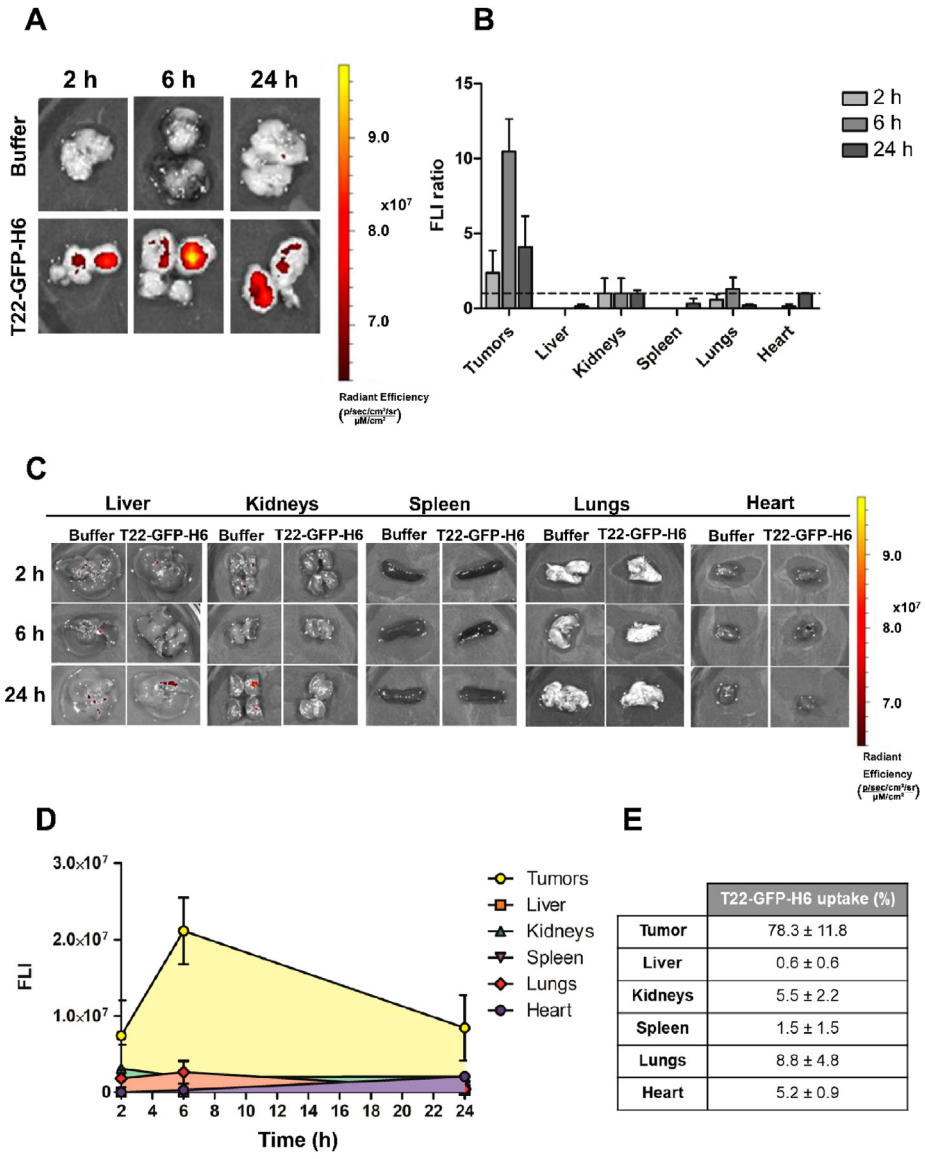

Figure 2 Biodistribution of the T22-GFP-H6 nanocarrier in a CXCR4-overexpressing subcutaneous HNSCC mouse model. (A) Representative images of emitted FLI signal in the 74B-CXCR4^{+} subcutaneous tumors 2, 6 or 24 h after the IV administration of either 200 μg of T22-GFP-H6 or buffer. (B) FLI ratio of the registered subcutaneous tumors and normal organs (liver, kidneys, spleen, lungs, and heart) at the three time points of the experiment (2, 6, and 24 h). FLI ratio was calculated by subtracting the FLI values of the buffer-treated mice (autofluorescence) and dividing the result by the FLI signal of the kidneys (organ chosen as reference). The dashed line indicates no change in FLI ratio (fold change = 1) (C) Representative images of the FLI registered in non-tumor tissues (liver, kidneys, spleen, lungs, and heart) 2, 6 or 24 h after the nanocarrier or buffer administration, (D) Area under the curve (AUC) of registered FLI through the time course of the experiment (2, 6, and 24 h) in the subcutaneous tumors and normal organs for the T22-GFP-H6 treated animals. (E) T22-GFP-H6 accumulation (%) by the subcutaneous tumors and non-tumoral tissues throughout the experiment. Percentages were calculated by dividing the emitted FLI of each organ (calculated by the AUC) between the total emitted FLI (sum of AUC of tumors and normal organs) and are represented as mean ± Standard error; $n = 3$ per group (total animal number 16). Statistical analysis performed by Student's *t*-test. FLI, fluorescence intensity.

expression levels. Moreover, no histological alterations were detected in the liver or kidneys (Fig. 3C), suggesting a lack of toxicity for the nanocarrier.

To further study T22-GFP-H6 *in vivo* kinetic behavior, the presence of circulating nanocarrier in plasma at different time points was studied after a single T22-GFP-H6 intravenous administration. FLI signal showed a first phase characterized by a fast biodistribution half-life ($t_{1/2} = \sim$20min) in plasma, followed by a second slow elimination phase, becoming practicaly undetectable after 2 h (Fig. 4). These results are consistent with previous findings in other tumor models[18,19].

3.3. T22-GFP-H6 exhibits a selective CXCR4 tumor distribution in subcutaneous HNSCC tumors

In order to further study T22-GFP-H6 CXCR4-dependant biodistribution, 74B mock and 74B-CXCR4^{+} tumor-bearing mice were administered an intravenous 200 μg dose of T22-GFP-H6.

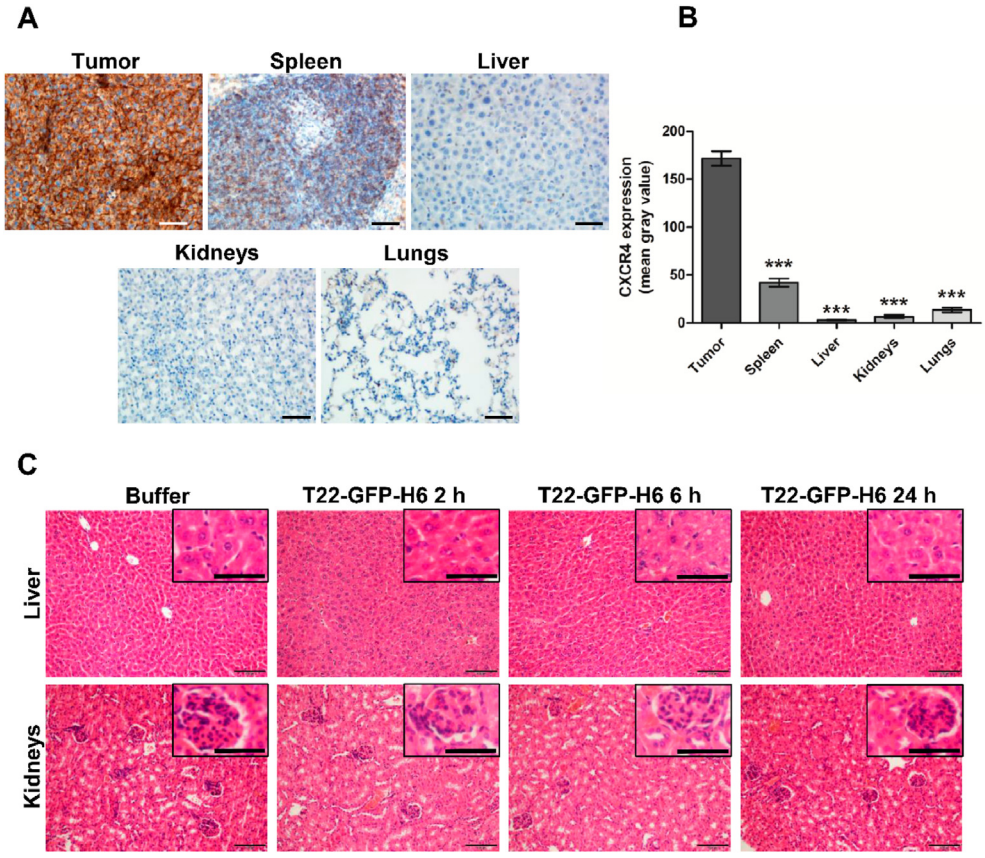

Figure 3 Immunohistochemical and histological analysis of tumors and non-tumor bearing organs from the T22-GFP-H6 biodistribution experiment. (A) Representative IHC images of the CXCR4 expression in tumor, spleen, liver, kidneys, and lungs. Scale bars = 50 μm (B) Quantification of the CXCR4 levels in tumors and normal organs (spleen, liver, kidneys, and lungs). CXCR4 expression was quantified as mean gray value and represented as mean ± Standard error, $n = 3$; ***$P < 0.001$. Statistical analysis performed by Student's *t*-test. (C) Histological analysis of liver and kidney sections stained with H&E from animals treated with either buffer or 200 μg T22-GFP-H6 for 2, 6, and 24 h. Scale bars = 100 or 50 μm (H&E zoom in).

Six hours post-treatment, time at which the FLI nanocarrier maximum accumulation was observed, animals were euthanized, and the fluorescence emitted by tumors and organs was registered. Results show that 74B-CXCR4$^+$ tumors accumulate significantly higher amounts of T22-GFP-H6 compared to 74B mock (Fig. 5A and B).

In addition, CXCR4-dependant biodistribution was confirmed by performing an AMD3100 blocking experiment. CXCR4$^+$ tumor-bearing mice were treated with three consecutive 10 mg/kg subcutaneous doses of AMD3100, one before T22-GFP-H6 intravenous injection, and two after. Animals were euthanized 6 h after T22-GFP-H6 administration, registering the emitted fluorescence as previously explained. AMD3100 administration during the T22-GFP-H6 treatment induced a statistically significant reduction in nanocarrier accumulation in tumors compared to those from animals that did not receive a prior treatment with the CXCR4 antagonist. Moreover, tumors of animals treated with both T22-GFP-H6 and AMD3100 presented a fluorescence intensity similar to those from buffer-treated mice, supporting a selective and CXCR4-dependant nanocarrier accumulation (Fig. 5A and B).

Consistently, 74B-CXCR4$^+$ tumors displayed a high CXCR4 membrane expression, as detected by IHC, whereas 74B mock tumors were negative for the receptor (Fig. 5C). These results confirm the selective CXCR4 tumor distribution of the nanocarrier.

T22-GFP-H6 CXCR4 selective tumor accumulation was further confirmed by GFP and CXCR4 co-immunofluorescence (Fig. 6). At the FLI maximum time point (6 h), T22-GFP-H6 (GFP staining) was detected within tumor tissue in the nanocarrier-treated animals, whereas their buffer-treated counterparts did not present any GFP signal. CXCR4 could be observed in all tumor cells from both groups, as 100% of 74B-CXCR4$^+$ cells expressed the receptor. Remarkably, nanocarrier-treated tumors presented a co-localization of T22-GFP-H6 and CXCR4 (yellow staining in merged images). This finding suggests that T22-GFP-H6 is able to interact with the CXCR4 receptor in the cell membrane leading to its internalization within CXCR4$^+$ HNSCC tumor cells. Importantly, no GFP signal was detected in liver or kidneys, further corroborating a selective T22-GFP-H6 accumulation in tumor tissue (Fig. 6). These results obtained by immunohistofluorescence are in agreement with our previous IVIS findings.

3.4. The incorporation of cytotoxic domains to the nanocarrier confers cytotoxic activity in CXCR4$^+$ subcutaneous HNSCC tumors without induction of systemic toxicity

To evaluate the ability of this T22-empowered nanocarrier platform to deliver cytotoxic agents into CXCR4-overexpressing HNSCC tumors, we took advantage of two nanotoxins, T22-

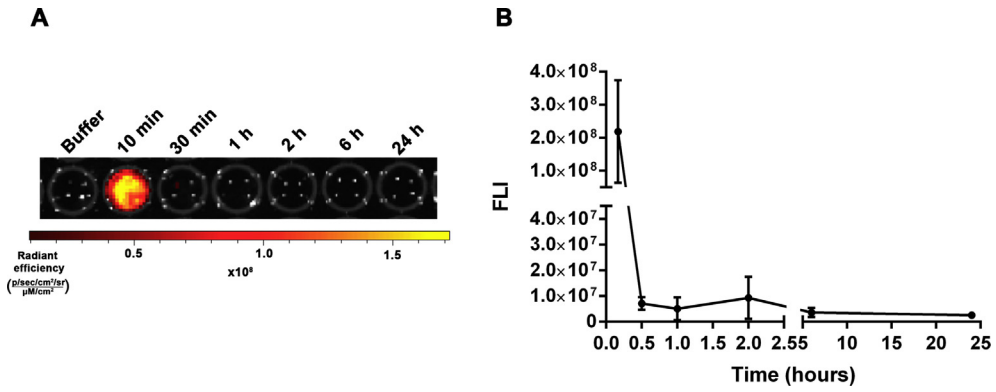

Figure 4 T22-GFP-H6 pharmacokinetics in plasma. (A) Representative images of the fluorescence signal (FLI) registered in plasma samples obtained at different times (buffer, 10 min, 30 min, 1, 2, 6, and 24 h) after T22-GFP-H6 administration. (B) Quantification of the fluorescence intensity (FLI) obtained from plasma samples through the time course of the experiment. Data represented as mean ± Standard error. $n = 3$ per time-point (total animal number 21).

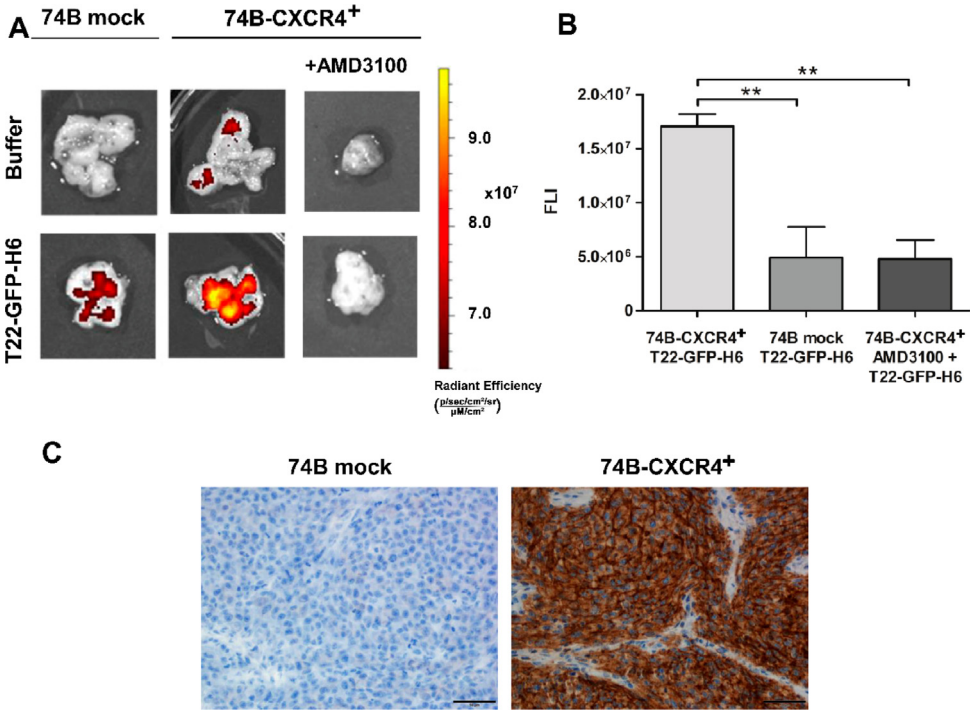

Figure 5 CXCR4-dependant T22-GFP-H6 tumor uptake by HNSCC subcutaneous tumors. (A) Representative FLI images of subcutaneous tumors generated by either the 74B mock or the 74B-CXCR4^{+} cell line 6 h after the IV administration of 200 µg of T22-GFP-H6, AMD3100^{+} T22-GFP-H6 or buffer. (B) FLI registered signal from the 74B mock or 74B-CXCR4^{+} subcutaneous tumors treated either with T22-GFP-H6 or the combination of the CXCR4 antagonist AMD3100 and T22-GFP-H6. (C) Immunohistochemical analysis of the CXCR4 expression in 74B mock and 74B-CXCR4^{+} subcutaneous tumors. Scale bar = 50 µm. Data represented as mean ± Standard error. $n = 3$ per group [total animal number 6 (biodistribution in 74B mock tumors) and 9 (biodistribution in 74B-CXCR4^{+} tumors pre-treated with AMD3100)]. $^{**}P < 0.01$. Statistical analysis performed by Student's *t*-test.

DITOX-H6, a protein nanoparticle including the diphtheria toxin catalytic domain, and T22-PE24-H6, which carries the *Pseudomonas aureoginosa* exotoxin A, both presenting a similar structure to T22-GFP-H6. Both toxins perform ADP-ribosylation of the ribosomal elongation factor 2 (EEF-2), leading to protein synthesis inhibition and cell death (Supporting Information Fig. S4). Firstly, we evaluated their cytotoxic effect in 74B mock and 74B-CXCR4^{+} HNSCC cell lines at three different time points (6, 24, and 48 h, Supporting Information Fig. S5A–S5C). Both nanotoxins were capable of inducing cell death at 24 h, reaching

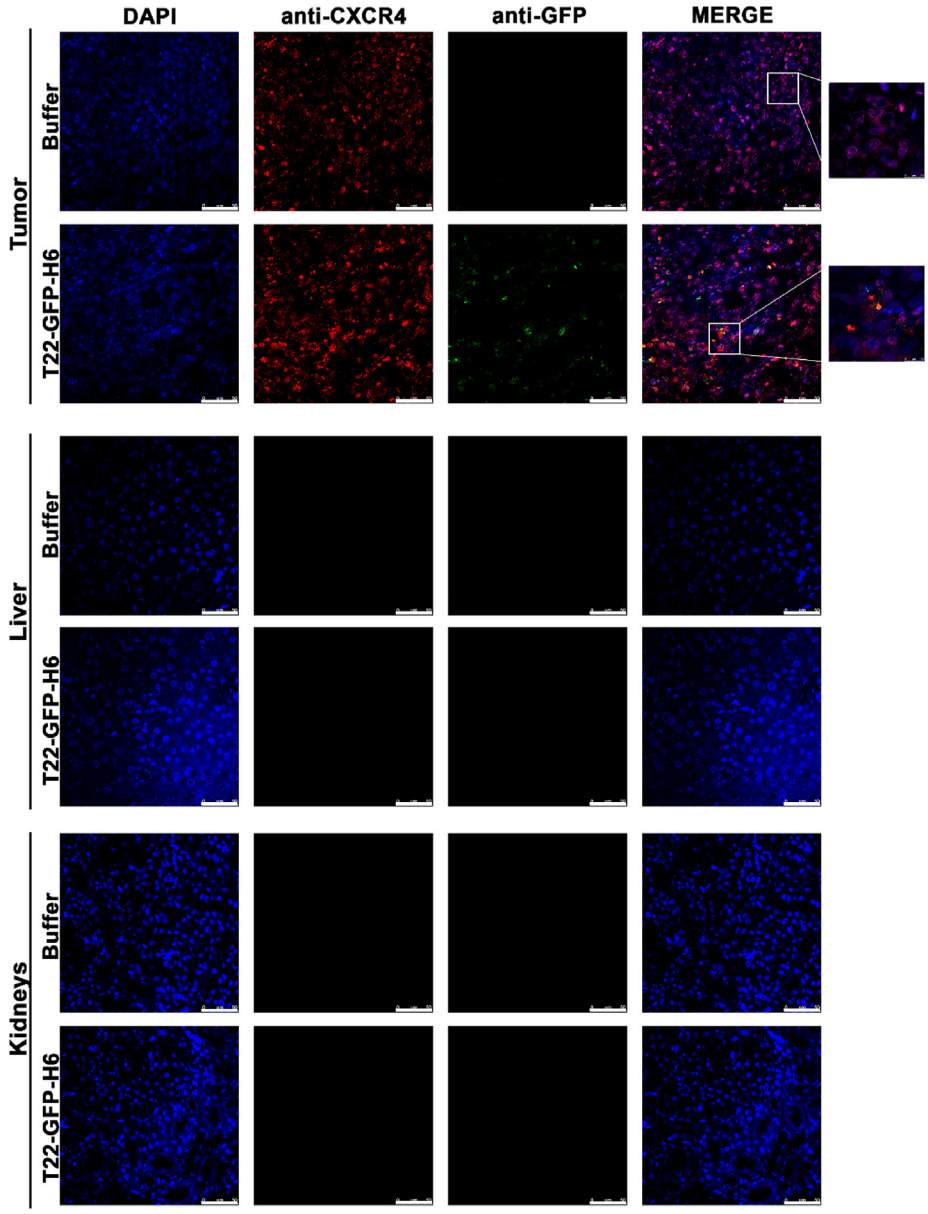

Figure 6 T22-GFP-H6 colocalizes with CXCR4$^+$ tumor cells after *in vivo* nanocarrier administration, while no GFP signal is detected in liver or kidneys. Representative immunofluorescence pictures of 74B-CXCR4$^+$ subcutaneous tumors, liver, and kidneys 6 h after the administration of either 200 μg of T22-GFP-H6 or buffer. T22-GFP-H6, detected by GFP staining, can be observed within the tumor tissue and colocalizing (yellow signal) with the CXCR4 receptor. On the other hand, no GFP staining was detected in liver or kidney tissue. DAPI staining (blue), anti-GFP (green), anti-CXCR4 (red), and merged images from the three channels. Scale bar = 50 or 10 μm (zoom in).

their full cytotoxicity after 48 h of exposure. Remarkably, both nanotoxins displayed a CXCR4-dependant cytotoxic effect, as 74B mock cells remained viable upon nanoparticle treatment. Moreover, to fully test the CXCR4-dependance of the cytotoxicity induced by both nanotoxins, supernatants from 74B-CXCR4$^+$ cells exposed to either T22-DITOX-H6 or T22-PE24-H6 for 48 h, were transferred to 74B mock cells. After 48 h of incubation, 74B mock cells remained viable, suggesting a lack of off-target cytotoxicity once the dead cells released their cellular content (Supporting Information Fig. S5D). These results indicate that no free toxin was present in the media, suggesting that the nanotoxins are degraded in the targeted cells after exerting their cytotoxic effect.

In order to further study T22-DITOX-H6 or T22-PE24-H6 cytotoxicity, 74B-CXCR4$^+$ subcutaneous tumor bearing mice were intravenously administered with a single dose of either 30 μg of T22-DITOX-H6 or 100 μg of T22-PE24-H6. After 24 or 48 h, time points at which we had observed cytotoxic effect *in vitro*, animals were euthanized, and tumors and normal organs were collected for their histological analysis. Both nanoparticles were able to induce cell death, as detected by DNA staining with DAPI, in tumor cells both at 24 and 48 h after treatment (Fig. 7A and B). Moreover, a tendency in the increase of dead cells at 48 h compared to 24 h could be observed in the tumors treated with both nanotoxins. These results were further confirmed by cleaved caspase-3 immunohistochemical staining, showing an increase of cleaved caspase-3 positive cells 48 h after nanotoxin administration (Fig. 7C and D).

In addition, no histopathological alterations were detected in liver or kidneys, as analyzed by H&E staining (Supporting

Information Fig. S6A). Moreover, no statistically significant differences in cell death (DNA staining) were observed in either of these organs in T22-DITOX-H6 and T22-PE24-H6-treated mice (Supporting Information Figs. S6B and S6C). These results suggest the suitability of the T22-GFP-H6 based nanocarrier platform to incorporate cytotoxic polypeptides of choice for their selective delivery to CXCR4$^+$ HNSCC cancer cells, reaching a potent cytotoxic effect in the absence of systemic toxicity.

3.5. T22-PE24-H6 and T22-DITOX-H6 nanotoxins induce a potent CXCR4-dependant antitumor effect in a CXCR4$^+$ orthotopic HNSCC mouse model in the absence of systemic toxicity

Finally, taking into account their great cytotoxic effect, we wanted to assess the antitumor effect of both T22-DITOX-H6 and T22-PE24-H6 nanotoxins. For this purpose, animals bearing either 74B mock or 74B-CXCR4$^+$ primary tumors (tongue), were daily administered with consecutive 10 μg intravenous doses of T22-DITOX-H6 or T22-PE24-H6 up to 5 doses. On alternate days, animals were weighed and tumor growth was determined by measuring the luminescent signal emitted by tumor cells using IVIS® Spectrum 200 system. Twenty-four hours after the last dose, animals were euthanized and tumors and organs were collected for further analysis.

Animals bearing 74B-CXCR4$^+$ primary tumors presented differences in tumor growth between groups (Fig. 8A). Nanotoxin-treated animals showed a decrease in tumor growth compared to their nanotoxin-treated counterparts (Fig. 8A). Primary tumor growth translated in a rapid body weight loss, which was more pronounced in animals from the buffer group compared to nanotoxin-treated animals (Fig. 8B). Ultimately, this weight loss determined the end of the experiment. Moreover, tumor volumes at the end point of the experiment were statistically significantly smaller in the nanotoxin-treated animals compared to the control group (Fig. 8C). Importantly, no antitumor effect was observed in the animals bearing 74B mock primary tumors, as no differences in tumor volume or body weight were detected between buffer and nanotoxin-treated animals (Supporting Information Fig. S7).

Lastly, no toxicity was observed by H&E staining in different organs, such as liver, kidneys, intestine, or bone marrow (Supporting Information Fig. S8A), suggesting a lack of toxicity for the treatment. This result is also consistent with the lower CXCR4 expression found in these organs compared to the primary tumor (Supporting Information Fig. S8B). Altogether these results support a potent CXCR4-dependant antitumor effect without leading to any histopathological alterations in non-tumor organs.

4. Discussions

Current HNSCC treatment still includes chemotherapeutic drugs, that affect all cells of the body since they are required to be administered at high doses in order to achieve significant antitumor effect. As a consequence, patients develop important systemic toxicities derived from the treatment[22]. In this context, nanoparticles have emerged in the last decades as promising vehicles for cancer management[23,24]. Nanoparticle size allows tumor accumulation through the fenestrations of tumor vasculature (EPR effect)[25,26]. Moreover, their bigger size compared to conventional small molecular tumor drugs, allows nanoparticles to avoid renal clearance increasing blood circulation time[25,27]. In theory, these facts enable nanoparticles to achieve a high tumor uptake lowering the drug dose, thus diminishing systemic toxicity. However, in reality, only 0.7% of the administered dose of the nanoparticles reported in the literature is able to reach the solid tumor, mainly accumulating (>95%) in other organs such as the liver, spleen, lungs, and kidneys resulting in hepatic and renal damage and systemic toxicity[25,28,29]. Remarkably, our results suggest otherwise, as the tumor accumulation was found to be higher than 75% of the administered dose, with less than 30% accumulation in other organs. These results were corroborated by GFP fluorescence detection and immunostaining. Moreover, normal histopathology of these organs suggests a lack of systemic toxicity, as T22-GFP-H6 mainly accumulates in tumors, avoiding adverse effects. These results are consistent with our previous findings in CRC and DLBCL cancer models[15,18], further confirming the suitability of T22-GFP-H6 as a promising nanocarrier in HNSCC.

The great performance of our nanocarrier might be at least partially explained by its organic composition. Many nanoparticles under research are made of inorganic materials which are poorly biocompatible and do not degrade easily, accumulating in organs such as liver and kidneys[30]. Moreover, these inorganic nanoparticles are coated with a protein corona when present in the body fluids, hindering their interaction with target cells[28,30–34]. Apart from its protein-only composition, T22-GFP-H6 nanocarrier presents other advantages such as its small size (around 13 nm), which is bigger than the renal filtration cut off (5−7 nm) but not big enough to be cleared out by macrophages, two big problems of current nanoparticles[25,27]. Importantly, the multivalency of the T22-GFP-H6 nanocarrier, that incorporates around twelve T22 ligands in each self-assembled nanoparticle, yields super-selectivity[35] that translates into selective internalization in HNSCC cells that overexpress the CXCR4 receptor, having negligible internalization in normal cells that lack or express low CXCR4 levels. These findings are consistent with the high receptor overexpression in tumors as compared to normal organs. Altogether, these facts might explain that less than 10% of the administered T22-GFP-H6 dose accumulates in liver and kidneys, without producing any histopathological damage.

Moreover, T22-GFP-H6 nanocarrier exploits the actively targeted strategy as a promising alternative to improve drug accumulation within tumor tissues[36,37]. Interestingly, the only clinical studies for HNSCC treatment involving fully protein nanoparticles are the EphB4-HSA fusion protein, an Ephrin-B2 ligand-receptor bound to albumin, and albumin-bound rapamycin (mTOR inhibitor)[38]. Antibody−drug conjugates (ADCs) represent another strategy for targeted drug delivery. However, it is estimated that <1% of the administered ADC dose is able to reach the tumor site, forcing the use of high doses which lead to important side effects and life-threatening toxicities. Due to these severe side effects and a limited improvement in efficacy compared to the free drug, 20 ADCs have been discontinued in the last decades. Moreover, ADCs also display a poor payload capacity, limited tumor uptake, and high toxicity[39,40]. Nevertheless, there are still more than 70 ADCs in clinical trials, that have been improved for instance using site-specific conjugation[41–43] or bi-specific targeting[44,45], for the treatment of several cancer types, including HNSCC[25]. Altogether, these facts highlight the current interest for nano-sized and targeted drug formulations, emphasizing the relevance of our protein-based nanoparticles targeting CXCR4.

Remarkably, our results showed a T22-GFP-H6 CXCR4-dependant internalization *in vitro*, as the nanocarrier did not

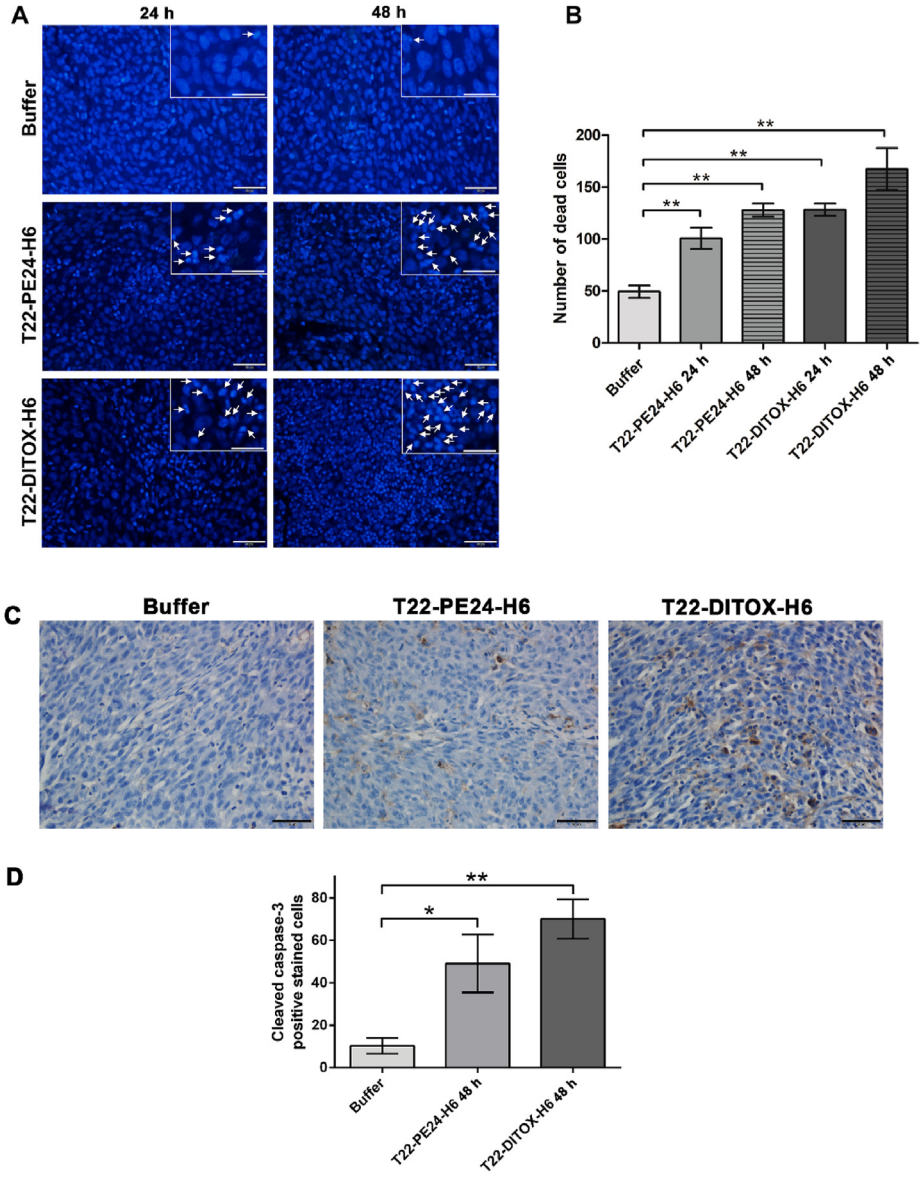

Figure 7 T22-PE24-H6 and T22-DITOX-H6 cytotoxic effect in a CXCR4$^+$ subcutaneous HNSCC animal model. (A) Detection of dead cells by condensate DNA staining (DAPI) in the 74B-CXCR4$^+$ subcutaneous tumors analyzed 24 or 48 h after the administration of a single dose of either T22-PE24-H6 or T22-DITOX-H6 nanotoxins. Scale bars = 50 or 25 μm (zoom in). (B) Quantification of the number of dead cells in the nanotoxin and buffer-treated tumors 24 and 48 h after treatment. (C) Immunohistochemical detection of cleaved caspase-3 in 74B-CXCR4$^+$ subcutaneous tumors 48 h after the administration of T22-PE24-H6 or T22-DITOX-H6. Scale bar = 50 μm. (D) Quantification of the number of cleaved caspase-3 positive stained cells in tumor tissue 48 h after treatment. Dead cells were detected by condensate DNA staining using DAPI and cleaved caspase-3 IHC. Data represented as mean ± Standard error. $n = 20$ per group (total number analyzed tissue sections per group). *$P < 0.05$; **$P < 0.01$. Statistical analysis performed by Student's t-test.

internalize in either CXCR4$^-$ cell lines or AMD3100 pre-treated CXCR4$^+$ HNSCC cell lines. Moreover, nanoparticle tumor distribution was enhanced by CXCR4 targeting as it was shown by two independent experiments. Firstly, the AMD3100 blocking experiment demonstrated a lower nanocarrier tumor accumulation in AMD3100-treated animals, compared to their non-treated counterparts. Correspondingly, CXCR4-non overexpressing tumor-bearing mice also presented significantly lower T22-GFP-H6 tumor accumulation than the ones overexpressing the receptor. Furthermore, immunofluorescence results showed a co-localization of CXCR4 and T22-GFP-H6, further confirming the interaction between the nanocarrier and the receptor.

Targeting CXCR4 has emerged as a promising strategy for cancer treatment, as it is associated with metastasis and worse prognosis in several solid tumors, including HNSCC. Moreover, CXCR4 has been described as a marker for metastatic cancer stem cells (CSC), a subset of cancer cells with capacity of self-renewal and differentiation that are responsible for the formation of tumor metastases[46–48]. Importantly, targeting the CXCR4 receptor to achieve targeted drug delivery is highly appealing since CXCR4 levels are much higher in tumor tissue compared to the normal organ in HNSCC, as well as other neoplasias[11,12]. Altogether, these results validate T22-GFP-H6 as a promising nanoparticle for HNSCC treatment, as previously described for other cancer

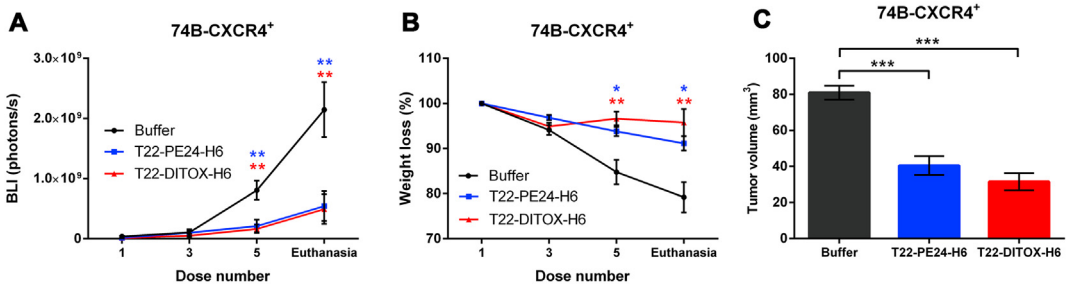

Figure 8 T22-PE24-H6 and T22-DITOX-H6 antitumor effect in a CXCR4$^+$ orthotopic HNSCC animal model. (A) Evolution of tumor growth in the three experimental groups (buffer, T22-PE24-H6, and T22-DITOX-H6) measured as luminescent signal emitted by tumor cells (BLI). (B) Variation of the body weight of buffer, T22-PE24-H6, and T22-DITOX-H6 treated animals represented as percentage of body weight loss. (C) Tumor volume registered at the end point of the experiment for the three experimental groups. Data represented as mean ± Standard error. $n = 5$ per group (total animal number 15). *$P < 0.05$; **$P < 0.01$; ***$P < 0.001$. Statistical analysis performed by Student's t-test. BLI, bioluminescence intensity (photons/s).

models[15,18]. Remarkably, to our knowledge, no protein-based nanocarrier for drug delivery has been described for the treatment of HNSCC, highlighting the relevance of this study.

Last but not least, the T22-GFP-H6 nanocarrier developed by our group has proved to be a versatile platform amenable to deliver drugs or cytotoxic polypetides, such as bacterial toxins, to selectively eliminate CXCR4$^+$ tumor cells[49–51]. Most CXCR4 therapies are based on small receptor inhibitors (*e.g.*, AMD3100), which have presented poor efficacy, especially in solid tumors[52]. Thus, current research is focused on the combination of blocking the CXCR4 pathway with other therapies, including chemotherapy, presenting promising results[10,52–54]. Nevertheless, these strategies still mainly rely on conventional chemotherapeutic drugs, which involve important systemic toxicities and undesired side effects for patients. Our approach goes a step further, creating protein-only nanoparticles with intrinsic cytotoxic activity by incorporating toxin domains. Following this strategy, we have developed the nanotoxins T22-PE24-H6 which incorporates an active fragment of *P. aeruginosa* exotoxin A, and T22-DITOX-H6 that includes an active fragment of the diphtheria toxin. Importantly, both nanotoxins were able to significantly induce cell death in tumor cells compared to buffer-treated mice in our CXCR4-overexpressing subcutaneous HNSCC model. In addition, T22-PE24-H6 and T22-DITOX-H6 achieved a potent CXCR4-dependant antitumor effect in a HNSCC orthotopic mouse model. Remarkably, treated mice did not present any histopathological alteration suggesting a lack of systemic toxicity for the treatment.

5. Conclusions

In conclusion, this study showed the selective internalization of the T22-GFP-H6 nanocarrier exclusively to CXCR4-overexpressing HNSCC cell lines. Moreover, upon intravenous administration in a HNSCC CXCR4-overexpressing subcutaneous mouse model, the nanocarrier mainly accumulates in tumor tissues (>75% of the administered dose) compared to non-tumor bearing organs. This result contrasts with previously reported nanoparticles by other groups, that presented a low tumor uptake. In addition, nanocarrier tumor accumulation is mediated by the CXCR4 receptor. This finding is consistent with the high CXCR4 expression reported in tumors, compared to normal tissues, including organs of the immune system, such as the spleen. Last but not least, this T22-empowered nanocarrier platform displays a great versatility to selectively deliver cytotoxic domains to CXCR4$^+$ HNSCC tumors, without inducing systemic toxicity. Altogether, these results validate the T22-GFP-H6 as a versatile platform to generate novel therapeutic nanoparticles, incorporating the small drug or the cytotoxic polypeptide of choice, to achieve the selective targeting and elimination of CXCR4$^+$ cells, involved in HNSCC metastatic dissemination, which represents one of the main causes of patient mortality. Thus, selective elimination of CXCR4$^+$ cells might represent a huge improvement in HNSCC therapy.

Acknowledgments

This work was supported by Instituto de Salud Carlos III (ISCIII, Spain; Co-funding from FEDER, European Union) [PI18/00650, PIE15/00028, PI15/00378 and EU COST Action CA 17140 to Ramon Mangues, PI19/01661 to Xavier León, and PI17/00584 to Miquel Quer]; Agencia Estatal de Investigación (AEI, Spain) and Fondo Europeo de Desarrollo Regional (FEDER, European Union) [grant BIO2016-76063-R, AEI/FEDER, UE to Antonio Villaverde and grant PID2019-105416RB-I00/AEI/10.13039/501100011033 to Esther Vázquez]; CIBER-BBN (Spain) [CB06/01/1031 and 4NanoMets to Ramon Mangues, VENOM4CANCER to Antonio Villaverde, NANOREMOTE to Esther Vázquez, and NANOSCAPE to Ugutz Unzueta]; AGAUR (Spain) 2017-SGR-865 to Ramon Mangues, and 2017SGR-229 to Antonio Villaverde; Josep Carreras Leukemia Research Institute (Spain) [P/AG to Ramon Mangues]. Elisa Rioja-Blanco and Laura Sánchez-García were supported by a predoctoral fellowship from AGAUR (Spain) (2020FI_B2 00168 and 2018FI_B2_00051) co-funded by European Social Fund (ESF investing in your future, European Union). Lorena Alba-Castellón was supported by a postdoctoral fellowship from AECC (Spanish Association of Cancer Research, Spain). Antonio Villaverde received an Icrea Academia Award (Spain). Ugutz Unzueta was also supported by Grant PERIS SLT006/17/00093 from la Generalitat de Catalunya (Spain) and Miguel Servet fellowship (CP19/00028) from Instituto de Salud Carlos III (Spain) co-funded by European Social Fund (ESF investing in your future, European Union). The bioluminescent follow-up of cancer cells and toxicity studies has been performed in the ICTS-141007 Nanbiosis Platform, using its CIBER-BBN Nanotoxicology Unit (http://www.nanbiosis.es/portfolio/u18-nanotoxicology-unit/). Protein production has been partially performed by the ICTS "NANBIOSIS", more specifically by the Protein Production Platform of CIBER-BBN/IBB (http://www.nanbiosis.es/unit/u1-protein-production-platform-ppp/).

Author contributions

We declare that all authors made fundamental contributions to the manuscript. Elisa Rioja-Blanco, Esther Vázquez, Ramon Mangues, Lorena Alba-Castellón, and Xavier León designed the study. Elisa Rioja-Blanco, Irene Arroyo-Solera, Ugutz Unzueta, and Isolda Casanova contributed in the development of the methodology. Elisa Rioja-Blanco, Irene Arroyo-Solera, Patricia Álamo, Naroa Serna, and Laura Sánchez-García adquired the data and carried out the experiments. Elisa Rioja-Blanco and Alberto Gallardo carried out the histopathological analysis. The analysis and interpretation of data was performed by Elisa Rioja-Blanco, Miquel Quer, Xavier León, Antonio Villaverde, Esther Vázquez, Ramon Mangues, and Lorena Alba-Castellón. Elisa Rioja-Blanco prepared the manuscript. Ugutz Unzueta, Isolda Casanova, Antonio Villaverde, Esther Vázquez, Ramon Mangues, and Lorena Alba-Castellón performed the manuscript reviews and revisions. The study was supervised by Esther Vázquez, Ramon Mangues, Lorena Alba-Castellón, and Xavier León. All authors revised the manuscript and approved the final version.

Conflicts of interest

Antonio Villaverde, Esther Vázquez, Ugutz Unzueta, Ramon Mangues, and Isolda Casanova are cited as inventors in PCT/EP2012/050513 covering Targeted delivery of therapeutic molecules to CXCR4 cells, and in PCT/EP2018/061732, covering Therapeutic Nanostructured Proteins. All other authors report no conflicts of interest in this work.

Appendix A. Supporting information

Supporting data to this article can be found online at https://doi.org/10.1016/j.apsb.2021.09.030.

References

1. Rothenberg SM, Ellisen LW. The molecular pathogenesis of head and neck squamous cell carcinoma. *J Clin Invest* 2012;**122**:1951−7.
2. Bray F, Ferlay J, Soerjomataram I, Siegel RL, Torre LA, Jemal A. Global cancer statistics 2018: GLOBOCAN estimates of incidence and mortality worldwide for 36 cancers in 185 countries. *CA - Cancer J Clin* 2018;**68**:394−424.
3. León X, Quer M, Orús C, Del Prado Venegas M, López M. Distant metastases in head and neck cancer patients who achieved locoregional control. *Head Neck* 2000;**22**:680−6.
4. Vokes EE, Agrawal N, Seiwert TY. HPV-associated head and neck cancer. *J Natl Cancer Inst* 2015;**107**:djv344.
5. Sacco AG, Cohen EE. Current treatment options for recurrent or metastatic head and neck squamous cell carcinoma. *J Clin Oncol* 2015;**33**:3305−15.
6. de Bree R, Senft A, Coca-Pelaz A, Kowalski L, Lopez F, Mendenhall W, et al. Detection of distant metastases in head and neck cancer: changing landscape. *Adv Ther* 2018;**35**:161−72.
7. Shi J, Kantoff PW, Wooster R, Farokhzad OC. Cancer nanomedicine: progress, challenges and opportunities. *Nat Rev Cancer* 2017;**17**:20−37.
8. Mangues R, Vázquez E, Villaverde A. Targeting in cancer therapies. *Med Sci* 2016;**4**:6.
9. Albert S, Riveiro ME, Halimi C, Hourseau M, Couvelard A, Serova M, et al. Focus on the role of the CXCL12/CXCR4 chemokine axis in head and neck squamous cell carcinoma. *Head Neck* 2013;**35**:1819−28.
10. Domanska UM, Kruizinga RC, Nagengast WB, Timmer-Bosscha H, Huls G, De Vries EGE, et al. A review on CXCR4/CXCL12 axis in oncology: no place to hide. *Eur J Cancer* 2013;**49**:219−30.
11. Knopf A, Bahadori L, Fritsche K, Piontek G, Becker C-C, Knolle P, et al. Primary tumor-associated expression of CXCR4 predicts formation of local and systemic recurrency in head and neck squamous cell carcinoma. *Oncotarget* 2017;**8**:112739−47.
12. León X, Diez S, García J, Lop J, Sumarroca A, Quer M, et al. Expression of the CXCL12/CXCR4 chemokine axis predicts regional control in head and neck squamous cell carcinoma. *Arch Oto-Rhino-Laryngol* 2016;**273**:4525−33.
13. Murakami T, Zhang T-Y, Koyanagi Y, Tanaka Y, Kim J, Suzuki Y, et al. Inhibitory mechanism of the CXCR4 antagonist T22 against human immunodeficiency virus type 1 infection. *J Virol* 2002;**76**.933−933.
14. Céspedes MV, Unzueta U, Tatkiewicz W, Sánchez-Chardi A, Conchillo-Solé O, Álamo P, et al. *In vivo* architectonic stability of fully *de novo* designed protein-only nanoparticles. *ACS Nano* 2014;**8**:4166−76.
15. Unzueta U, Céspedes MV, Ferrer-Miralles N, Casanova I, Cedano J, Corchero JL, et al. Intracellular CXCR4$^+$ cell targeting with T22-empowered protein-only nanoparticles. *Int J Nanomed* 2012;**7**:4533−44.
16. Unzueta U, Ferrer-Miralles N, Cedano J, Zikung X, Pesarrodona M, Saccardo P, et al. Non-amyloidogenic peptide tags for the regulatable self-assembling of protein-only nanoparticles. *Biomaterials* 2012;**33**:8714−22.
17. López-Laguna H, Unzueta U, Conchillo-Solé O, Sánchez-Chardi A, Pesarrodona M, Cano-Garrido O, et al. Assembly of histidine-rich protein materials controlled through divalent cations. *Acta Biomater* 2019;**83**:257−64.
18. Falgàs A, Pallarès V, Unzueta U, Céspedes MV, Arroyo-Solera I, Moreno MJ, et al. A CXCR4-targeted nanocarrier achieves highly selective tumor uptake in diffuse large B-cell lymphoma mouse models. *Haematologica* 2020;**105**:741−53.
19. Sánchez-García L, Serna N, Álamo P, Sala R, Céspedes MV, Roldan M, et al. Self-assembling toxin-based nanoparticles as self-delivered antitumoral drugs. *J Control Release* 2018;**274**:81−92.
20. Brenner JC, Graham MP, Kumar B, Saunders LM, Kupfer R, Lyons RH, et al. Genotyping of 73 UM-SCC head and neck squamous cell carcinoma cell lines. *Head Neck* 2010;**32**:417−26.
21. Zhao M, Sano D, Pickering CR, Jasser SA, Henderson YC, Clayman GL, et al. Assembly and initial characterization of a panel of 85 genomically validated cell lines from diverse head and neck tumor sites. *Clin Cancer Res* 2011;**17**:7248−64.
22. Pérez-Herrero E, Fernández-Medarde A. Advanced targeted therapies in cancer: drug nanocarriers, the future of chemotherapy. *Eur J Pharm Biopharm* 2015;**93**:52−79.
23. Petros RA, Desimone JM. Strategies in the design of nanoparticles for therapeutic applications. *Nat Rev Drug Discov* 2010;**9**:615−27.
24. Wagner V, Dullaart A, Bock AK, Zweck A. The emerging nanomedicine landscape. *Nat Biotechnol* 2006;**24**:1211−7.
25. Serna N, Sánchez-García L, Unzueta U, Díaz R, Vázquez E, Mangues R, et al. Protein-based therapeutic killing for cancer therapies. *Trends Biotechnol* 2018;**36**:318−35.
26. Haley B, Frenkel E. Nanoparticles for drug delivery in cancer treatment. *Urol Oncol Semin Orig Investig* 2008;**26**:57−64.
27. Zhou Q, Dong C, Fan W, Jiang H, Xiang J, Qiu N, et al. Tumor extravasation and infiltration as barriers of nanomedicine for high efficacy: the current status and transcytosis strategy. *Biomaterials* 2020;**240**:119902.
28. Wilhelm S, Tavares AJ, Dai Q, Ohta S, Audet J, Dvorak HF, et al. Analysis of nanoparticle delivery to tumours. *Nat Rev Mater* 2016;**1**:16014.
29. Bae YH, Park K. Targeted drug delivery to tumors: myths, reality and possibility. *J Control Release* 2011;**153**:198−205.
30. Naahidi S, Jafari M, Edalat F, Raymond K, Khademhosseini A, Chen P. Biocompatibility of engineered nanoparticles for drug delivery. *J Control Release* 2013;**166**:182−94.

31. Xiao W, Gao H. The impact of protein corona on the behavior and targeting capability of nanoparticle-based delivery system. *Int J Pharm* 2018;**552**:328−39.
32. Ke PC, Lin S, Parak WJ, Davis TP, Caruso F. A decade of the protein corona. *ACS Nano* 2017;**11**:11773−6.
33. Miceli E, Kar M, Calderón M. Interactions of organic nanoparticles with proteins in physiological conditions. *J Mater Chem B* 2017;**5**: 4393−405.
34. Salvati A, Pitek AS, Monopoli MP, Prapainop K, Bombelli FB, Hristov DR, et al. Transferrin-functionalized nanoparticles lose their targeting capabilities when a biomolecule corona adsorbs on the surface. *Nat Nanotechnol* 2013;**8**:137−43.
35. Liu M, Apriceno A, Sipin M, Scarpa E, Rodriguez-Arco L, Poma A, et al. Combinatorial entropy behaviour leads to range selective binding in ligand-receptor interactions. *Nat Commun* 2020;**11**:4836.
36. Lammers T, Kiessling F, Ashford M, Hennink W, Crommelin D, Strom G. Cancer nanomedicine: is targeting our target?. *Nat Rev Mater* 2016;**1**:1−2.
37. Danhier F, Feron O, Préat V. To exploit the tumor microenvironment: passive and active tumor targeting of nanocarriers for anti-cancer drug delivery. *J Control Release* 2010;**148**:135−46.
38. Clinicaltrials.gov. Search for clinical trials in head and neck squamous cell carcinoma. Available from: https://clinicaltrials.gov. [Accessed 9 March 2021].
39. Masters JC, Nickens DJ, Xuan D, Shazer RL, Amantea M. Clinical toxicity of antibody drug conjugates: a meta-analysis of payloads. *Invest N Drugs* 2018;**36**:121−35.
40. Donaghy H. Effects of antibody, drug and linker on the preclinical and clinical toxicities of antibody-drug conjugates. *mAbs* 2016;**8**:659−71.
41. Junutula JR, Raab H, Clark S, Bhakta S, Leipold DD, Weir S, et al. Site-specific conjugation of a cytotoxic drug to an antibody improves the therapeutic index. *Nat Biotechnol* 2008;**26**:925−32.
42. Yamada K, Ito Y. Recent chemical approaches for site-specific conjugation of native antibodies: technologies toward next-generation antibody−drug conjugates. *Chembiochem* 2019;**20**:2729−37.
43. Schumacher D, Hackenberger CPR, Leonhardt H, Helma J. Current status: site-specific antibody drug conjugates. *J Clin Immunol* 2016;**36**:100−7.
44. Maruani A. Bispecifics and antibody−drug conjugates: a positive synergy. *Drug Discov Today Technol* 2018;**30**:55−61.
45. Shim H. Bispecific antibodies and antibody−drug conjugates for cancer therapy: technological considerations. *Biomolecules* 2020;**10**.
46. Dalerba P, Clarke MF. Cancer stem cells and tumor metastasis: first steps into uncharted territory. *Cell Stem Cell* 2007;**1**:241−2.
47. Miki J, Furusato B, Li H, Gu Y, Takahashi H, Egawa S, et al. Identification of putative stem cell markers, CD133 and CXCR4, in hTERT-immortalized primary nonmalignant and malignant tumor-derived human prostate epithelial cell lines and in prostate cancer specimens. *Cancer Res* 2007;**67**:3153−61.
48. Faber A, Goessler UR, Hoermann K, Schultz JD, Umbreit C, Stern-Straeter J. SDF-1-CXCR4 axis: cell trafficking in the cancer stem cell niche of head and neck squamous cell carcinoma. *Oncol Rep* 2013;**29**: 2325−31.
49. Céspedes MV, Unzueta U, Aviñó A, Gallardo A, Álamo P, Sala R, et al. Selective depletion of metastatic stem cells as therapy for human colorectal cancer. *EMBO Mol Med* 2018;**10**:e8772.
50. Falgàs A, Pallarès V, Serna N, Sánchez-García L, Sierra J, Gallardo A, et al. Selective delivery of T22-PE24-H6 to CXCR4^{+} diffuse large B-cell lymphoma cells leads to wide therapeutic index in a disseminated mouse model. *Theranostics* 2020;**10**:5169−80.
51. Pallarès V, Unzueta U, Falgàs A, Sánchez-García L, Serna N, Gallardo A, et al. An Auristatin nanoconjugate targeting CXCR4^{+} leukemic cells blocks acute myeloid leukemia dissemination. *J Hematol Oncol* 2020;**13**:36.
52. Guo F, Wang Y, Liu J, Mok SC, Xue F, Zhang W. CXCL12/CXCR4: a symbiotic bridge linking cancer cells and their stromal neighbors in oncogenic communication networks. *Oncogene* 2016:816−26.
53. Chen K, Huang YH, Chen JL. Understanding and targeting cancer stem cells: therapeutic implications and challenges. *Acta Pharmacol Sin* 2013;**34**:732−40.
54. Hermann PC, Huber SL, Heeschen C. Metastatic cancer stem cells: a new target for anti-cancer therapy?. *Cell Cycle* 2008;**7**:188−93.